Multimodal Sensing Transparent Droplet Probe for Characterization of Superhydrophobic Surfaces

Arthur Vieira and Quan Zhou, *Member, IEEE*

***Abstract*—Natural and artificial superhydrophobic surfaces are a rapidly growing topic in both academia and industry due to their unique properties and applications. Numerous techniques have been developed to characterize the wetting properties of such surfaces, such as the optical contact angle goniometer, force-based methods, and microscopic techniques for visualizing the wetting interface. However, a method that combines nN resolution force measurement with direct observation of the wetting interface on opaque superhydrophobic surfaces is missing. Here, we report a high-sensitivity multimodal force-sensing transparent droplet probe for the characterization of superhydrophobic surfaces that allows simultaneous visualization of the wetting interface and measurement of interaction forces. The probe is composed of a transparent glass cantilever with a droplet probe attached to its end. During the interaction with the sample, the wetting interface is directly imaged through the probe, illuminated with coaxial lighting. The interaction force is simultaneously measured as the deflection of the cantilever-shaped probe. By combining top view, side view, and high-resolution force sensing, the probe can reveal force contributions from both surface tension and Laplace pressure and measure super-repellent surfaces with contact angles near 180° with a low experimental uncertainty of 0.5°.**

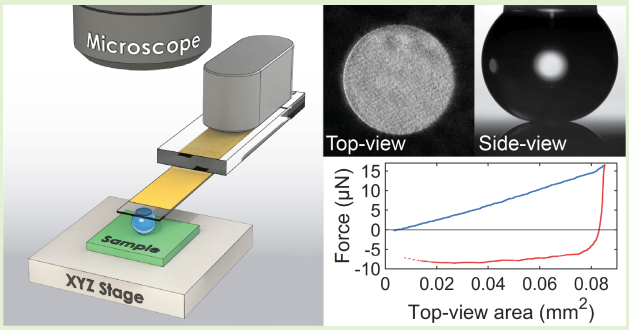

***Index Terms*— Droplet, force measurement, multimodal sensor, superhydrophobic, wetting characterization, wetting interface.**

I. Introduction

WATER-REPELLENT surfaces are ubiquitous in nature, such as lotus leaves [1], rose petals [2], and insect wings [3]. A wide variety of artificial surfaces have also been created for applications such as self-cleaning [4], antifogging [5], anti-icing [6], and energy harvesting [7]. These surfaces often contain chemical or topographical inhomogeneities, such as irregular roughness or surface coating. The resulting wetting interface is often complex, with trapped air pockets and irregular contact lines [8], where the state of the interface is also dependent on the history of the interaction [9].

Manuscript received 6 June 2023; accepted 18 June 2023. Date of publication 26 June 2023; date of current version 1 August 2023. This work was supported by Multidisciplinary Doctoral Study through Aalto Doctoral School of Electrical Engineering and the Academy of Finland under Grant #331149. The associate editor coordinating the review of this article and approving it for publication was Dr. Yong Zhu. *(Corresponding author: Quan Zhou.)*

The authors are with the Department of Electrical Engineering and Automation, School of Electrical Engineering, Aalto University, 02150 Espoo, Finland (e-mail: arthur.vieira@aalto.fi; quan.zhou@aalto.fi).

Digital Object Identifier 10.1109/JSEN.2023.3288333

Many surface-wetting characterization techniques have been developed, from the classical contact angle goniometer to different force-based instruments. Contact angle goniometry (CAG) is a gold standard given its ease of use but cannot visualize the interface. Moreover, when the surface is super-repellent or not flat, CAG becomes increasingly unreliable [10]. Force-based methods are also commonly used in wetting characterization for measuring either lateral friction forces during motion [11] or oscillation [12], or vertical adhesion forces [13], [14]. These techniques are easy to apply and provide a direct quantitative measure from which important wetting quantities can be derived, e.g., work of adhesion [13], [15] or wetting maps of the surfaces [14]. The force-based methods can also be highly sensitive, e.g., techniques based on atomic force microscopy (AFM) can achieve 20 pN force sensitivity and $\sim$1 μm lateral resolution in wetting characterization [16]. However, despite impressive advances in resolution, those force-based methods cannot accurately relate the force to advancing and receding contact angles of the surface and the exact contact line interactions

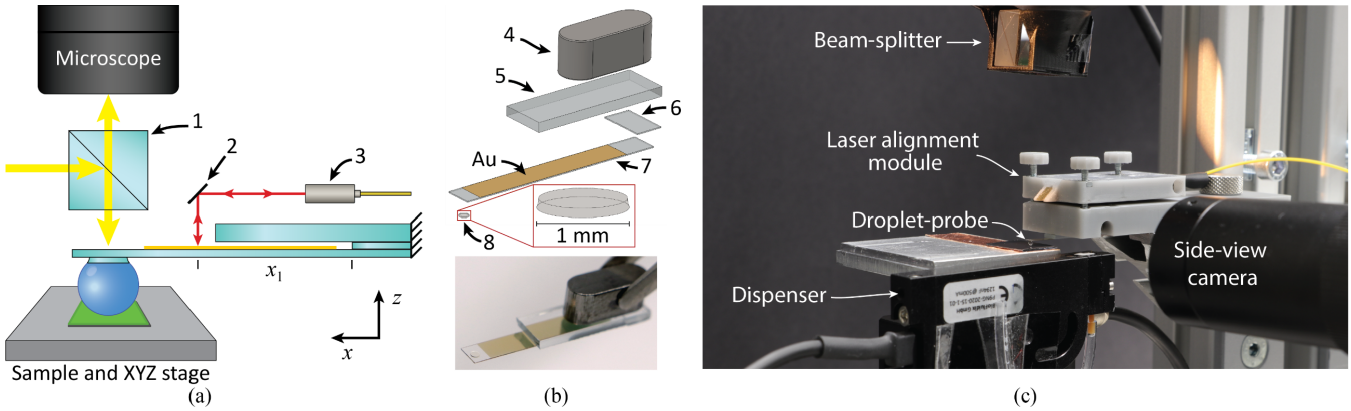

Fig. 1. Transparent droplet probe system. (a) Schematic of the transparent probe system. A transparent probe in the shape of a cantilever holds a liquid droplet. A top-view microscope images the wetting interface through the droplet. 1—beam splitter. 2—first surface gold mirror. 3—laser displacement sensor head. The location where the laser shines is marked x_1, measured relative to the base of the cantilever. (b) Exploded view of the individual pieces that compose the probe and photograph of the assembled probe. 4—steel mount piece. 5—protective glass cover. 6—glass spacer. 7—gold coated probe holding cantilever. 8—undercut disk for holding the droplet. (c) Close-up of experimental setup. The liquid droplet probe is held over a silicon nanograss sample piece.

associated with force events, except in very special cases such as on model pillar surfaces.

On the other hand, many methods have been used to image the wetting interface, such as environmental scanning electron microscopy (ESEM) [17], X-ray tomography [18], and AFM in imaging mode [19]. Nonetheless, only a few techniques are suitable for imaging the advancing and receding contact line. Bottom-view methods, such as laser scanning confocal microscopy [20] and reflective interference contrast microscopy [21], are probably the most fruitful techniques, but those methods require the sample to be transparent and cannot be applied when the sample is opaque, which is the property of the majority of water-repellent surfaces. Top-view methods have also been proposed for wetting characterization, especially in the hydrophilic regime, to measure contact line roundness and calculate contact angle from interface diameter and volume [22], [23]. On the other hand, those techniques are not reliable in the phobic regime due to contact line occlusion [24]. Through-droplet imaging techniques in the superhydrophobic regime have also been proposed for imaging the interface [25], [26]. Recently, promising results of through-droplet imaging using a transparent droplet probe have been reported [27] to directly image the contact interface and measure the advancing and receding contact angles on superhydrophobic surfaces. The method accurately estimates contact angles using the Young–Laplace relation during the measurement by precisely measuring the droplet's shape. However, a method that directly relates force measurement and advancing and receding contact angles is still missing.

Here, we present a force-sensing transparent droplet probe for multimodal characterization of super-repellent surfaces. The technique combines through-droplet imaging, side-view imaging, and high-resolution force-sensing to characterize super-repellent surfaces that can precisely distinguish the contributions of the contact line tension and Laplace forces, determine the phases of the wetting, and link forces and contact angles.

This article is organized as follows. Section II introduces the structure and working mechanism of the sensing system. Section III describes the design of the transparent droplet probe and Section IV explains the design of the optical system. Section V discusses the force-sensing mechanism and measurement procedure. Section VI describes the multimodal measurements combining vision and force. Section VII concludes this article.

II. System Overview

The force-sensing transparent droplet probe is a two-modal system, using both optical observation and force measurement. The key components of the system are shown in Fig. 1(a). The top-view optical observation is achieved with a transparent droplet probe, which can hold a spatially well-confined millimeter-sized droplet as the probing end-effector interacting with the sample surface. The interaction of the droplet and the sample surfaces, e.g., the state of the contact line and contact area, is observed using a top-view microscope and camera. A beam splitter is placed between the objective of the microscope and the transparent probe, allowing a white light source to illuminate the droplet–sample interface coaxially with the camera. To measure the deflection of the cantilever probe, a laser interferometer measures the displacement of the droplet-holding cantilever through a fixed reflection mirror. The droplet–sample interaction forces are then calculated from the deflection of the cantilever. The sample is mounted on an *XYZ* precision motorized stage, allowing precise and repeatable droplet–sample interaction. A noncontact droplet dispenser is mounted on the side of the *XYZ* sample stage and supplies liquid to form and maintain the droplet probe.

III. Transparent Droplet Probe

The transparent droplet probe is a key element of the system. The design of the probe aims to achieve two objectives: 1) to allow a stable and repeatable observation of the wetting interface and 2) to provide the measurement of the interaction force.

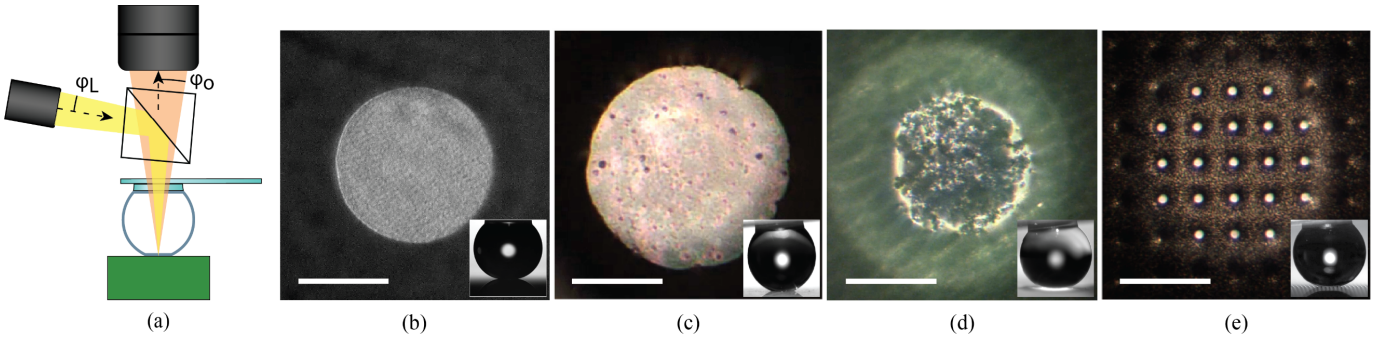

Fig. 2. Coaxial illumination and sample images from different measurements. (a) Coaxial illumination schematic. A point in the interface is illuminated by the light source with an illumination angle φ_L. Light is reflected from the illuminated point is captured by the objective with acceptance angle φ_o. (b) Silicon nanograss sample. (c) Glaco commercial coating. (d) Maranta plant leaf. (e) Silicon micropillars. (Scale bars: 200 μm.)

To perform precise and repeatable measurements, wetting characterization devices need to have some form of liquid stabilization, such as holding the droplet at the end of a dispensing needle. Stabilizing the droplet is especially important for superhydrophobic samples where droplets readily roll off [4]. To hold and accurately manipulate the liquid droplet and allow optical observation, we employ a transparent disk with a 1 mm diameter. The disk has an undercut edge that confines the droplet-wetting surface to the perimeter of the disk [28], forming a well-defined boundary. The disk is in turn attached to the end of a transparent glass cantilever, shown in Fig. 1(b), providing a stable optical interface for the top-view camera to image through (see Appendix I for detailed probe fabrication steps).

To form the droplet probe, we use a noncontact dispenser (PipeJet, BioFluidix GmbH, Germany) to dispense purified water (Direct-Q 3UV-R water purification system, Millipore SAS, France) from beneath onto the underside of the disk. The dispenser is attached to the side of the motorized sample stage, allowing precise alignment beneath the disk and automatic refilling. To form the droplet probe, smaller droplets of approximately 5-nL volume are dispensed sequentially. Before each measurement, the volume of the droplet probe is set to 1.5 μL, in line with our previous works [14], [27]. This volume is a compromise between the effects of gravity and evaporation. The diameter of the droplet corresponding to this volume is 1.44 mm, well below the capillary length of water of 2.7 mm, such that the effects of gravity over its shape are insignificant. The droplet should also be sufficiently large that evaporation effects are insignificant throughout a measurement. An evaporation rate of around 1.8 nL/s has been observed under normal ambient conditions or 3% volume reduction during a typical 25 s measurement.

IV. Optical System

The optical system is designed as a compromise between four main criteria: 1) an objective with a sufficiently small acceptance angle to resolve the contact line; 2) a sufficiently large field-of-view to image the whole contact interface; 3) a sufficiently high resolution that can observe small changes on the interfacial contact line and area; and 4) a sufficiently large working distance to accommodate the instrument components.

The illumination strategy exploits the reflective nature of the interface to achieve contrast between the droplet–sample interface and the droplet sidewalls. Most superhydrophobic surfaces exhibit an air layer or pockets of air at the interface between the droplet and the rough surface, also known as plastron. The ability of the surface to retain this air layer is key to the water-repelling properties of the surface [8].

The maximum slope angle of the plastron at which light will reflect into the camera is defined by the combination of the illumination angle of the light source, φ_L, and acceptance angle of the objective, φ_o [see Fig. 2(a)]. A collimated white light source (OSL2 with collimating lens OSL2COL, Thorlabs Inc., USA) is reflected through a beam splitter (15 mm 50R/50T, Edmund Optics Inc., USA) mounted between the cantilever and the probe, which illuminates the droplet–sample interface coaxially to the camera. The light source is placed approximately 150 mm away and has an 11 mm radius aperture, resulting in an illumination angle of $\varphi_L \simeq 2.1°$. A microscope with a magnification of 6× is used to provide a full view of the wetting interface (VZM 600i, Edmund Optics Inc., USA, and a color camera BFS-U3-28S5C C or grayscale camera BFS-U3-28S5M C, Flir LLC). The field-of-view is approximately 1.1 × 1.1 mm^2 at a working distance of 60 mm and a pixel resolution of ∼750 nm/px. A large working distance is preferred as it minimizes the angular aperture, $\varphi_o \simeq 7.0°$, while also providing the space between the camera and the probe for other components.

The maximum slope angle of the plastron at which light will partially reflect into the camera is $(\varphi_o + \varphi_L)/2 \simeq \pm 4.6°$ and fully reflected into the camera is $(\varphi_o - \varphi_L)/2 \simeq \pm 2.5°$. This slope angle is small enough to image the plastron while providing a margin to account for the sample mounting angle and variations in the flatness of the plastron. To prevent direct reflection from optical components, in particular the walls of the beam splitter, we tilt the light source by 10° and the beam splitter by 5°.

The performance of the illumination and vision system was evaluated on four different samples: fluoropolymer-coated silicon nanograss [Fig. 2(b)]; Glaco-coated glass slide (Mirror Coat Zero, Soft99 Company) [Fig. 2(c)]; a Maranta plant leaf (Leuconeura Amabilis Mint) [Fig. 2(d)]; and silicon

micropillars (20 μm diameter, 60 μm spacing, and 50 μm height) [Fig. 2(e)]. The optical properties of each sample influence the appearance of the wetting interface (see Appendix II for details of sample fabrication/preparation).

In general, if the dry surface is light-absorbing or reflective, the plastron will show high contrast. However, if the surface scatters light, the light reflected from the plastron may provide less contrast against the scattered light. For such samples, the probe may be tilted, e.g., by 5.5° to improve the contrast. Fig. 2(b)–(e) shows the examples of the sample images. Dry silicon nanograss [Fig. 2(b)] is black under the naked eye and the plastron appears with great contrast. On the Glaco sample, Fig. 2(c), the wetting interface also shows high contrast despite the reflective nature of the dry Glaco surface. Light reflected outside the interface does not reach the objective. On the other hand, on the Maranta leaf, Fig. 2(d), the plastron shows bright discontinuous regions, attributed to heterogeneous surface composition and roughness of the surface. The rest of the surface appears green due to scattered light. On the silicon micropillars, Fig. 2(e), the droplet is in contact with the top of 21 pillars but does not touch the bottom of the pillars, also known as the Cassie state [29]. In this case, the wetted pillar tops appear bright relative to other pillars. The trapped air layer accounts for only a limited amount of brightness in the image, with some light also scattering from the rough surface at the bottom of the pillars.

V. Force Measurement System

The droplet probe is also designed to measure the wetting forces, where the design is centered around a compromise between force resolution and time response. During interaction with a water-repellent sample, a millimeter-sized droplet experiences wetting forces that range from tens of μN down to and below 1 nN, and wetting events occur at the millisecond scale [14]. The interaction forces bend the cantilever-shaped glass probe, where the deflection is measured by a nanometer resolution laser interferometer (model IDS3010 with fiberoptic sensor head D4/F17, Attocube Systems AG, Germany) shining through a 45° mirror, as shown in Fig. 1(a). The laser head and mirror are assembled on a custom tilt stage, as shown in Fig. 1(c). The alignment between the laser and the cantilever is achieved by maximizing the laser signal intensity while adjusting the three screws on the tilt stage.

Fig. 3(a) shows a typical force curve acquired at 50 kHz, used to characterize the performance of the force sensor. During the approach, the sample is raised toward the droplet. The sample contacts the droplet at approximately 0.7 s, from which the force gradually increases up to ~18.9 μN. At around 11 s, the sample stage reverses and the force decreases. From ~18.4 s, the droplet experiences negative forces due to adhesion to the surface. Finally, the droplet detaches in an abrupt event at ~23.9 s.

The deflection profile of the cantilever under the droplet–sample interaction forces, $D(x)$, can be derived from the Euler–Bernoulli beam theory (1). The cantilever's elastic constant k relates a force acting at the center of the droplet-holding disk, $x = l$, to the vertical displacement at the same

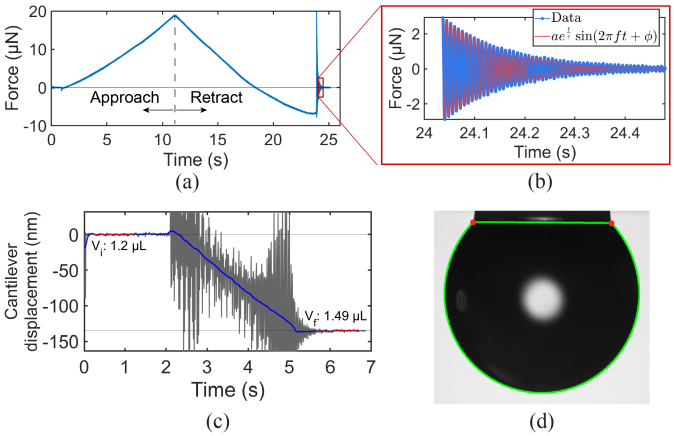

Fig. 3. Force measurement and calibration. (a) Example force measurement. During the approach, the sample is pressed against the droplet and during retraction the droplet is depressed. (b) Force signal after the droplet detaches from the sample, as a function of time. Decaying exponential is fit. (c) Calibration data. Gray—raw force sensor data. Blue—filtered force sensor data. Red—initial and final force values. Initial and final volumes are also shown. The uncalibrated force is recorded during the dispensing. (d) Volumes are estimated from side-view image, both before and after dispensing. Red dots mark the corners of the disk and green line outlines the droplet profile used to estimate the volume.

location, see (2). We measure l as the distance from the base of the cantilever to the center of the droplet-holding disk

$$D(x) = \frac{2F}{Et^3w}\left(3lx^2 - x^3\right) \tag{1}$$

$$k = \frac{F}{D(l)} = \frac{Et^3w}{4l^3} \tag{2}$$

where E is Young's modulus of the glass and w and t are the width and thickness of the cantilever, respectively.

The force signal calibration k_t relates the displacement, $D(x_1)$, to the force, F, acting on the droplet, where x_1 is the distance from the base of the cantilever to the laser measurement site, as shown in Fig. 1(a)

$$F = k_t D(x_1), \quad k_t = \alpha k. \tag{3}$$

For the camera to have a clear view over the disk, the laser interferometer needs to be aligned further back in the cantilever, as shown in Fig. 1(a). The difference in vertical displacement at the disk and the measurement site is accounted for by α, which can be estimated as $\alpha = D(l)/D(x_1)$.

The hydrolytic class 1 glass cantilever has an average $E \simeq 70$ GPa with dimensions of $l \simeq 18.45$ mm, $w \simeq 2.8$ mm, and $t \simeq 110$ μm. In our setup, $\alpha \simeq 1.81$ leading to an expected calibration constant of $k_t = 18.8$ N/m, for a force acting at the center of the droplet-holding disk. The force measurement range is limited by the alignment tolerance angle of the interferometer laser head on a perpendicular surface, specified as ±0.3°. The deflection angle along the cantilever, $\varphi(x)$, is derived from (1)

$$\varphi(x) = -\tan^{-1}\left(\frac{6F}{Et^3w}\left(2lx - x^2\right)\right). \tag{4}$$

Using the same parameters, the expected maximum measurable force range is ±700 μN under the assumption

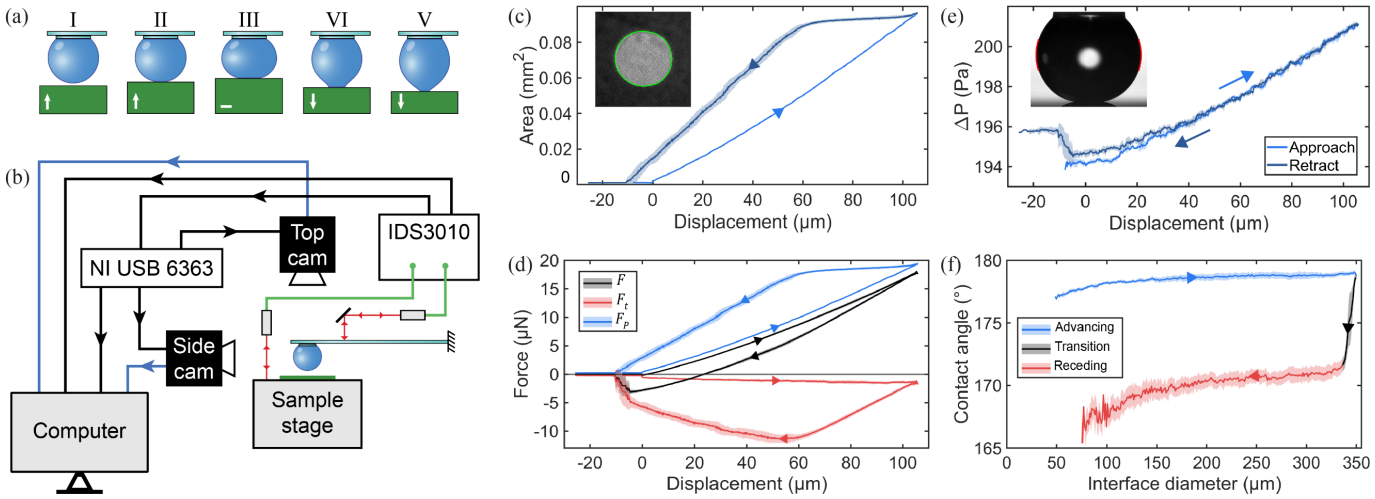

Fig. 4. Multimode acquisition combining top view, side view, and force measurements. (a) Measurement process. I—droplet probe is placed above the measurement site. II—sample stage moves upward, and the sample contacts the probe, resulting in an initial contact area. III—sample stage reverses direction. IV—sample stage moves downward decompressing the droplet. V—sample stage moves further downward, and the interface area reduces until the droplet is detached from the sample surface. (b) Simplified wiring schematic for the experimental setup (see Fig. 1(c) for the physical position of the system components). Blue lines represent video signals, green lines represent optical fibers, and black lines represent digital and analog signals. (c) Interface area as a function of sample stage displacement. Inset shows the top view, where the green outline represents the contact line identified by machine vision. (d) Forces as a function of sample stage displacement. Black: total force measured F. Red: force due to surface tension acting on contact line F_t. Blue: force due to Laplace pressure acting on interface area F_P. (e) Laplace pressure $_1P$ as a function of sample stage displacement, measured with machine vision from the side view. Inset shows the side view of droplet during the experiment, where red lines show the segment of the droplet edge used in fitting. (f) Contact angle as a function of interface diameter. Blue: contact line is advancing. Black: contact line resists movement. Red: contact line recedes. (Solid lines represent the mean value and shaded area represents the standard deviation.)

that the laser is perfectly aligned. It is worth noting that the maximum working range of the cantilever is ∼1.3 mN when the cantilever touches the protective cover.

To calibrate the force sensor, we increase the volume of the droplet on the probe leading to a measurable displacement due to the known change in weight. An example calibration force curve is shown in Fig. 3(c). The volumes are estimated based on side-view image analysis of pictures taken before and after refilling, Fig. 3(d). The change in weight of the droplet is used to calibrate the effective elastic constant of the cantilever. For the example case of Fig. 3(c), the resulting calibration value is 20.9 N/m. This constant depends on the cantilever and installation and is calibrated per experiment, where typical values range from 15 to 25 N/m.

To estimate the resolution of the force measurement, we analyzed the force signal over 30 independent 1-s periods, while the probe was not touching the sample and the setup is idle. The mean of the standard deviations of the displacement is 0.19 nm, leading to a force resolution of ∼3.9 nN, at 100-Hz acquisition speed.

To estimate the settling time t_s and the frequency of resonance f, we model the cantilever with the disk and 1.5-μL droplet as a second-order system. Upon the droplet detaching from the sample, the probe experiences an abrupt transition from approximately -6 to 0 μN, shown in Fig. 3(b), i.e., a step stimulus in force. The subsequent oscillation shows that the system is underdamped, for which the step response can be approximated as a decaying sinusoid

$$ae^{t/\tau}\sin(2\pi f t+\varphi) \tag{5}$$

where a is the initial amplitude, τ is the decaying time constant, f is the damped frequency of resonance, and φ is the phase of the oscillation. By fitting the oscillation with (5), we determine $f \simeq 128$ Hz and $t_s = 4\tau \simeq 0.49$ s (2% tolerance band). During the wetting experiments, the droplet probe is mostly quasi-static while in contact with the sample surface. The half-second settling time after the droplet detaches from the surface is acceptable.

VI. Multimode Measurement

In multimode measurements, the optical measurements and force measurements provide different perspectives of the experiments. The top-view images provide detailed information on how the contact line advances and recedes, such as pinning/depinning at surface imperfections, which might not be resolved in the force signal. Top-view images can also provide visual evidence of any changes to the interior of the interface, such as the Cassie–Wenzel transition [29], which is marked by the loss of reflectivity of the interface due to the collapse of the plastron. On the other hand, the force measurement provides a quantitative measure of important wetting quantities such as snap-in and pull-off forces (the moment when the droplet touches and detaches from the sample) or other wetting events that can be associated with visual changes in the interface.

A typical measurement consists of pressing and depressing the sample against the droplet [see Fig. 4(a)]. First, the droplet is aligned above the measurement site. During the approach phase, the sample stage is raised toward the droplet with a velocity of 10 μm/s until the droplet is pressed by approximately 100 μm. Then, the sample stage reverses its motion

direction and retracts at the same speed until the droplet detaches from the surface. Before each measurement, the droplet is brought into contact with an electrically grounded piece of nanograss to remove electrostatic charges, which may otherwise affect the measurement.

The simplified wiring schematic for the setup is shown in Fig. 4(b). In multimode acquisition, the top- and side-view cameras operate at 100 fps, triggered by a DAQ board (NI USB 6363, National Instruments Inc., USA). The laser interferometer is used to measure the force signals as well as the Z displacement of the sample stage, also acquired at 100 Hz. The same DAQ board acquires the laser interferometer force signal as well as sample stage displacement during measurement to ensure signal synchronization. Timestamps are used to synchronize the images from the cameras to the sample stage and force signals.

An example of multimode measurement performed in silicon nanograss is shown in Fig. 4(c)–(e). Five consecutive measurements were made on the same sample location, from which the mean and standard deviations were calculated (solid and shaded area, respectively).

The interface area is shown in Fig. 4(c) as a function of sample stage displacement. The top-view images are post-analyzed in MATLAB to find the area of the interface in each frame of the measurement. For each frame, a binary image was produced by threshold. The area of the interface is calculated as the area of the largest filled blob. The displacement axis was set to zero at snap-in (the moment when the droplet first contacts the sample).

Fig. 4(d) shows the forces acting at the interface. The total measured force F is shown in black, which can be decomposed as the sum of the water–air surface tension force F_t acting on the perimeter of the wetting interface and the force due to Laplace pressure F_P acting on the interface area

$$F = \underbrace{L_{\mathrm{CL}}\gamma \sin(\theta_c)}_{F_t} - \underbrace{A\Delta P}_{F_P} \tag{6}$$

where L_{CL} is the contact line perimeter length, obtained through machine vision (green line in Fig. 4(c) inset); γ is the liquid surface tension; θ_c is the average contact angle of the droplet with the interface; A is the interface area, shown in Fig. 4(c); and ΔP is the Laplace pressure.

To estimate ΔP, we measure the radii of curvature using side-view images [Fig. 4(e), inset] using the Laplace pressure equation

$$\Delta P = \gamma\left(\frac{1}{R_1} + \frac{1}{R_2}\right) \tag{7}$$

where R_1 and R_2 are the principal radii of curvature at any point of the air–water interface of the droplet. R_1 is estimated as the mean of the radii on each side of the droplet, which are obtained by fitting a circle to a segment of the edge of the droplet, detected with a binary threshold (red curves in Fig. 4(e), inset). R_2 is estimated as the horizontal half-width of the droplet.

The mean contact angle θ_c from the five measurements is shown in Fig. 4(f) as a function of interface diameter. The contact angle can be calculated from (6) by combining the top-view measurement of A and L_{CL}, side-view measurement of ΔP, and force sensor measurement of F. Three characteristic wetting phases can be identified: the advancing phase, shown in blue, during which the sample stage is raised toward the droplet. During this phase, the interface area grows and the contact line advances over the surface with an approximately constant contact angle. The transition phase, shown in black, starts after the sample stage reverses direction. The end of the transition phase was determined from the slope of θ_c. During the transition phase, the contact line remains pinned and the area is approximately constant. The receding phase follows, shown in red, as the sample stage continues to move downward. During the receding phase, the interface area decreases continuously, and the contact angle is approximately constant. The mean advancing contact angle is $178.5° \pm 0.5°$ and the mean receding angle is $169.9° \pm 1.3°$, where the uncertainties correspond to the standard deviation. We note that these are experimental uncertainties, where the contact angle noise was estimated to be 0.04° as the standard deviation of ten 1-s periods taken evenly along the contact angle measurement.

VII. Summary and Discussion

In this article, we present a force-sensing transparent droplet probe for the multimodal characterization of superhydrophobic surfaces. A liquid droplet is held at the end of a glass cantilever, while a top-view camera images the droplet–sample interface through the droplet. The glass cantilever doubles as a force sensor, which enables the simultaneous recording of droplet–sample interaction forces. The top-view images are analyzed with machine vision to obtain a continuous measurement of the interface area.

The multimodal measurement provides valuable opportunities to directly measure the state of the wetting interface. Force components from both surface tension and Laplace pressure can be measured separately. The contact angle of super-repellent surfaces can also be calculated with a great resolution by combining top view, side view, and high-resolution force sensing. These data may better inform material scientists and wetting researchers on how to better characterize and develop superhydrophobic materials. Other lighting strategies can also be explored, such as the use of polarizing filters and even fluorescence microscopy. Moreover, the transparent probe can also be applied to other optical microscopes, such as the laser scanning confocal microscope, to provide detailed 3-D imaging of the interface.

Appendix I
Probe Fabrication

The components used to fabricate the probe are shown in Fig. 1(b). The 22 × 2.8 mm cantilever and 5 × 2.8 mm spacers are cut from a #0 glass coverslip (∼110 μm thickness) and the 20 × 5 × 1 mm protective probe cover is cut from a glass slide. All glass pieces are cut using a Disco DAD3220 dicing machine.

The back of the cantilever is coated with gold using a Cressington 108 auto sputter device, with care not to coat over the disk region and the back side where it will be glued to the probe.

A 10 × 4 × 4 mm stainless steel piece is assembled to the top of the glass protective cover to facilitate manipulation and mounting, with the help of a screw and a magnet.

To fabricate the undercut disks, a 100-μm-thick layer of SU-8 50 was spin-coated (1500 rpm, 30 s) on a silicon oxide coated wafer followed by 15 min at 95 °C soft bake on a hotplate, 20-s UV exposure using a Karl Suss MA6 mask aligner, 15-min post-exposure bake at 95 °C, and then development in PGMEA for 20 min. The disks were manually released using a scalpel. A microgripper was used to precisely place the disk on the cantilever glass piece at approximately 0.25 mm from the end of the glass slide.

All parts were assembled with UV curable optical glue, model Delo Photobond GB310, Delo.

Appendix II
Samples

The two silicon nanograss samples used were produced by a maskless cryogenic deep reactive ion etching process using an Oxford Plasmalab System 100 on a 4-in silicon wafer (⟨100⟩, p-type boron doped, >1 Ω cm). The process parameters were 1000 W of ICP forward power, a temperature of −110 °C, 10 mTorr of pressure, and 7 min of etching time. For the nanograss in Fig. 2(b), the flow rates were: SF_6 40.0 sccm and O_2 18.0 sccm. For the nanograss in Figs. 3 and 4, the flow rates were SF_6 32.9 sccm and O_2 25.1 sccm.

The Glaco sample in Fig. 2(c) was prepared by coating a microscope glass slide with Glaco Mirror Coat Zero spray (Soft99 Company) at room conditions. The sample was set on its side and let to dry.

The Maranta potted plant (Leuconeura Amabilis Mint), shown in Fig. 2(d), was purchased from local sellers. A test sample of the leaf was cut using scissors and attached to a glass slide using double-sided tape. The test sample was washed with purified water prior to measurement and let to dry for approximately 5 min.

The silicon micropillars in Fig. 2(e) were fabricated by cryogenic deep reactive ion etching with a silicon dioxide hard mask. The starting substrate was a ⟨100⟩ silicon wafer with 500-nm wet thermal oxide. The micropillar pattern was defined by UV lithography (AZ5214 photoresist, Süss MA6 mask aligner). The oxide was etched with reactive ion etching using an Oxford Plasmalab 80+ (Oxford Instruments, Bristol, U.K.), 18-min etching time, 200-mTorr pressure, 30-W power, 25-sccm CHF_3, and 25-sccm Ar flows. The photoresist was then stripped by ultrasonication in acetone for 10 min. Next, the micropillars were etched using an Oxford Plasmalab 100 (Oxford Instruments, Bristol, U.K.). The micropillars were fabricated with anisotropic silicon etch (O_2 6 sccm, SF_6 40 sccm, forward power 3 W, ICP power 1050 W, 110 °C temperature, 8-mtorr pressure, and 24-min etching time). Afterward, the oxide mask was stripped in buffered HF, and the etch depth was determined by a profilometer (Bruker Dektak XT) to be 50 μm. The diameter of the pillars was 20 μm, and the pillars were in a square array with 60-μm spacing.

References

[1] W. Barthlott and C. Neinhuis, "Purity of the sacred lotus, or escape from contamination in biological surfaces," *Planta*, vol. 202, no. 1, pp. 1–8, Apr. 1997, doi: 10.1007/s004250050096.

[2] B. Bhushan and M. Nosonovsky, "The rose petal effect and the modes of superhydrophobicity," *Phil. Trans. Roy. Soc. A, Math., Phys. Eng. Sci.*, vol. 368, no. 1929, pp. 4713–4728, Oct. 2010, doi: 10.1098/rsta.2010.0203.

[3] T. Wagner, C. Neinhuis, and W. Barthlott, "Wettability and contaminability of insect wings as a function of their surface sculptures," *Acta Zoologica*, vol. 77, no. 3, pp. 213–225, Jul. 1996, doi: 10.1111/j.1463-6395.1996.tb01265.x.

[4] R. Fürstner, W. Barthlott, C. Neinhuis, and P. Walzel, "Wetting and self-cleaning properties of artificial superhydrophobic surfaces," *Langmuir*, vol. 21, no. 3, pp. 956–961, Feb. 2005, doi: 10.1021/la0401011.

[5] Y. Lai et al., "Transparent superhydrophobic/superhydrophilic TiO_2-based coatings for self-cleaning and anti-fogging," *J. Mater. Chem.*, vol. 22, no. 15, p. 7420, 2012, doi: 10.1039/c2jm16298a.

[6] M. J. Kreder, J. Alvarenga, P. Kim, and J. Aizenberg, "Design of anti-icing surfaces: Smooth, textured or slippery?" *Nature Rev. Mater.*, vol. 1, no. 1, p. 15003, Jan. 2016, doi: 10.1038/natrevmats.2015.3.

[7] H. Wu, N. Mendel, D. van den Ende, G. Zhou, and F. Mugele, "Energy harvesting from drops impacting onto charged surfaces," *Phys. Rev. Lett.*, vol. 125, no. 7, Aug. 2020, Art. no. 078301, doi: 10.1103/PhysRevLett.125.078301.

[8] A. Lafuma and D. Quéré, "Superhydrophobic states," *Nature Mater.*, vol. 2, no. 7, pp. 457–460, Jul. 2003, doi: 10.1038/nmat924.

[9] L. Gao and T. J. McCarthy, "Contact angle hysteresis explained," *Langmuir*, vol. 22, no. 14, pp. 6234–6237, Jul. 2006, doi: 10.1021/la060254j.

[10] M. Vuckovac, M. Latikka, K. Liu, T. Huhtamäki, and R. H. A. Ras, "Uncertainties in contact angle goniometry," *Soft Matter*, vol. 15, no. 35, pp. 7089–7096, 2019, doi: 10.1039/C9SM01221D.

[11] D. W. Pilat, P. Papadopoulos, D. Schäffel, D. Vollmer, R. Berger, and H.-J. Butt, "Dynamic measurement of the force required to move a liquid drop on a solid surface," *Langmuir*, vol. 28, no. 49, pp. 16812–16820, Dec. 2012, doi: 10.1021/la3041067.

[12] M. Junaid, H. A. Nurmi, M. Latikka, M. Vuckovac, and R. H. A. Ras, "Oscillating droplet tribometer for sensitive and reliable wetting characterization of superhydrophobic surfaces," *Droplet*, vol. 1, no. 1, pp. 38–47, Jul. 2022, doi: 10.1002/DRO2.9.

[13] B. Samuel, H. Zhao, and K.-Y. Law, "Study of wetting and adhesion interactions between water and various polymer and superhydrophobic surfaces," *J. Phys. Chem. C*, vol. 115, no. 30, pp. 14852–14861, Aug. 2011, doi: 10.1021/jp2032466.

[14] V. Liimatainen et al., "Mapping microscale wetting variations on biological and synthetic water-repellent surfaces," *Nature Commun.*, vol. 8, no. 1, pp. 1–7, Nov. 2017, doi: 10.1038/s41467-017-01510-7.

[15] D. Daniel et al., "Mapping micrometer-scale wetting properties of superhydrophobic surfaces," *Proc. Nat. Acad. Sci. USA*, vol. 116, no. 50, pp. 25008–25012, Dec. 2019, doi: 10.1073/pnas.1916772116.

[16] D. Daniel, Y. Florida, C. L. Lay, X. Q. Koh, A. Sng, and N. Tomczak, "Quantifying surface wetting properties using droplet probe atomic force microscopy," *ACS Appl. Mater. Interface*, vol. 12, no. 37, pp. 42386–42392, Sep. 2020, doi: 10.1021/acsami.0c12123.

[17] A. T. Paxson and K. K. Varanasi, "Self-similarity of contact line depinning from textured surfaces," *Nature Commun.*, vol. 4, no. 1, pp. 1–8, Feb. 2013, doi: 10.1038/ncomms2482.

[18] S. Yang et al., "Direct insight into the three-dimensional internal morphology of solid-liquid-vapor interfaces at microscale," *Angew. Chem. Int. Ed.*, vol. 54, no. 16, pp. 4792–4795, Apr. 2015, doi: 10.1002/anie.201411023.

[19] M. Moosmann, T. Schimmel, W. Barthlott, and M. Mail, "Air–water interface of submerged superhydrophobic surfaces imaged by atomic force microscopy," *Beilstein J. Nanotechnol.*, vol. 8, pp. 1671–1679, Aug. 2017, doi: 10.3762/bjnano.8.167.

[20] A. Naga, A. Kaltbeitzel, W. S. Y. Wong, L. Hauer, H.-J. Butt, and D. Vollmer, "How a water drop removes a particle from a hydrophobic surface," *Soft Matter*, vol. 17, no. 7, pp. 1746–1755, 2021, doi: 10.1039/d0sm01925a.

[21] Y. Jiang, Y. Sun, J. W. Drelich, and C.-H. Choi, "Topography-dependent effective contact line in droplet depinning," *Phys. Rev. Lett.*, vol. 125, no. 18, Oct. 2020, Art. no. 184502, doi: 10.1103/PhysRevLett.125.184502.

[22] T. S. Meiron, A. Marmur, and I. S. Saguy, "Contact angle measurement on rough surfaces," *J. Colloid Interface Sci.*, vol. 274, no. 2, pp. 637–644, Jun. 2004, doi: 10.1016/j.jcis.2004.02.036.

[23] G. Dutra, C. Martelli, and J. Canning, "Simple top down imaging measurement of contact angle for practical assessment of hydrophilic surfaces," *Proc. SPIE*, vol. 9655, Jul. 2015, Art. no. 96550S, doi: 10.1117/12.2185249.

[24] F. Geyer et al., "When and how self-cleaning of superhydrophobic surfaces works," *Sci. Adv.*, vol. 6, no. 3, pp. 1–12, Jan. 2020, doi: 10.1126/sciadv.aaw9727.

[25] C. Luo et al., "Direct three-dimensional imaging of the buried interfaces between water and superhydrophobic surfaces," *Angew. Chem.*, vol. 122, no. 48, pp. 9331–9334, Nov. 2010, doi: 10.1002/ange.201002470.

[26] B. Haimov, S. Pechook, O. Ternyak, and B. Pokroy, "Shape of water–air interface beneath a drop on a superhydrophobic surface revealed: Constant curvature that approaches zero," *J. Phys. Chem. C*, vol. 117, no. 13, pp. 6658–6663, Apr. 2013, doi: 10.1021/jp312650f.

[27] A. Vieira, W. Cui, V. Jokinen, R. H. A. Ras, and Q. Zhou, "Through-drop imaging of moving contact lines and contact areas on opaque water-repellent surfaces," *Soft Matter*, vol. 19, no. 13, pp. 2350–2359, 2023, doi: 10.1039/D2SM01622B.

[28] V. Liimatainen, V. Sariola, and Q. Zhou, "Controlling liquid spreading using microfabricated undercut edges," *Adv. Mater.*, vol. 25, no. 16, pp. 2275–2278, Apr. 2013, doi: 10.1002/adma.201204696.

[29] D. Quéré, "Wetting and roughness," *Annu. Rev. Mater. Res.*, vol. 38, no. 1, pp. 71–99, Aug. 2008.

Arthur Vieira received the M.Sc. degree in physics engineering from the Faculty of Sciences, University of Lisbon, Lisbon, Portugal, in 2017. He is currently pursuing the Ph.D. degree in physics engineering with the Robotic Instruments Group, Aalto University, Espoo, Finland.

He has been developing surface-wetting characterization instrumentation for water-repellent surfaces based on liquid droplet probing. His research interests include liquid–solid interfacial phenomena, microrobotics and micromanipulation, soft matter manipulation, and automation and visual servoing control.

Quan Zhou (Member, IEEE) received the M.Sc. degree in control engineering and the Dr.Tech. degree in automation technology from the Tampere University of Technology, Tampere, Finland, in 1996 and 2004, respectively.

He is a Full Professor leading the Robotic Instrument Group at the Department of Electrical Engineering and Automation, School of Electrical Engineering, Aalto University, Finland. His main research interests include miniaturized robotic instruments, micromanipulation, and related automation methods.

Dr. Zhou was the General Chair of the International Conference on Manipulation, Automation and Robotics at Small Scales, MARSS 2019. He was also the Chair of the IEEE Finland Joint Chapter of the Control System Society, the Robotics and Automation Society, and the System Man and Cybernetics Society. He is currently a Coordinator of the Miniaturized Robotics Topic Group of the European Robotics Association (euRobotics). He was also a Coordinator of EU FP7 Project FAB2ASM, the first PPP Project of the European Economic Recovery Plan.